FISEVIER

Contents lists available at ScienceDirect

Journal of Luminescence

journal homepage: http://www.elsevier.com/locate/jlumin

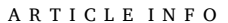


Full Length Article

Photoelectric properties of Sr₂MgSi₂O₇: Eu²⁺ phosphors produced by co-precipitation method

Su-Hua Yang a, **, Hwa-Yu Lee a, Po-Chang Tseng A, Ming-Hsien Lee

- ^a Department of Electronic Engineering, National Kaohsiung University of Science and Technology, Kaohsiung, 80778, Taiwan, ROC
- ^b Department of Physics, Tamkang University, New Taipei City, 25137, Taiwan, ROC



Keywords: Sr₂MgSi₂O₇:Eu²⁺ Blue phosphor Density functional theory (DFT) CASTEP Latent fingerprint (LFP)

ABSTRACT

Eu $^{2+}$ -doped phosphors $Sr_2MgSi_2O_7$: xEu^{2+} (x=1–5 mol%) with blue color are synthesized by the coprecipitation method. The X-ray diffraction patterns of these phosphors indicate a tetragonal crystal structure. The emission peak centered at 486 nm is attributed to the 4 $F^7 \rightarrow 4F^65D^1$ transitions of Eu^{2+} ions with CIE coordinates of (Eu^{2+} ions with CIE coordinates of (Eu^{2+} ions on different surfaces under 337 nm UV light. The results indicate that this phosphor may possess the potential to be used for LFP recognition. Three calculated models mimicking the crystal host, Eu^{2+} ion-doped phosphor, and Eu^{2+} ion-doped phosphor with oxygen vacancy are built using CASTEP software to perform density functional theory (DFT) calculations. The geometry optimization results of the Eu^{2+} doping ion reveal that a coordinate covalent bond is formed by the Eu^{2+} doping ion with its neighboring oxygen atoms. The oxygen vacancy Eu^{2+} ions.

1. Introduction

Long afterglow phosphors have great potential for application in many fields such as lighting [1–3], traffic signs [4,5], watches and clocks [6,7], luminous paints [8], sensors and detectors [9,10], biomedical imaging [11,12], photocatalysis [13,14], and solar cells [15,16]. Among various kinds of phosphors, silicates can be used in a wide range of applications due to their easy preparation [17], low cost [18], stable crystal structure [19], long persistence time [20–22], physical and chemical stabilities [23,24], excellent water resistance [25], environment friendliness [26], varied luminescent colors [27], and strong absorption in the near-UV region.

The family of materials $M_2MgSi_2O_7$ (M=Ca, Sr, Ba), which are called alkaline earth akermanites, are the most widely studied persistent luminescent silicates [28–34]. Ions of rare earth elements are the most common doped ion to be used as an activator in phosphors. Luminescent Eu^{2+} ions can emit light from the UV to the infrared region on different host matrices because the involved 5d orbital of a Eu^{2+} ion is external and strongly influenced by the crystal field. Activator Eu^{2+} ions are used to make $Sr_2MgSi_2O_7$ based blue phosphors, and their broadband

emission usually consists of transitions from $4f^65\ d^1$ to the $4f^7$ ground state.

The host of $Sr_2MgSi_2O_7$ (SMSO) has a tetragonal crystal structure. The Sr^{2+} ion in this crystal structure occupies a position that is connected with eight neighboring O^{2-} ions. Obviously, when Eu^{2+} is doped into the SMSO crystal, the electronic structure of SMSO is not changed because their ionic radii are almost the same, and no charge compensation is required for the replacement of Sr^{2+} with Eu^{2+} . Therefore, we adopted the density functional theory (DFT) calculation in the Cambridge Sequential Total Energy Package (CASTEP) software and used a simple primitive crystal model to study how the Eu^{2+} doping and oxygen vacancies affect the electronic orbitals in the crystal structure.

Among the various synthesis methods, the co-precipitation method [35–53] is known to produce phosphor powders with uniform, narrow size distribution, and a homogeneous distribution of the activator ions. Therefore, the co-precipitation method was chosen to prepare $\rm Sr_2MgSi_2O_7$: $\rm Eu^{2+}$ phosphors with various doping concentrations of $\rm Eu^{2+}$ ions. According to our experimental results, the optimum $\rm Eu^{2+}$ doping concentration was 4 mol%, and the optimum sintered temperature and time were 1150 °C and 11 h, respectively.

E-mail addresses: shya@nkust.edu.tw (S.-H. Yang), lettie0602@gmail.com (H.-Y. Lee).



^{*} Corresponding author.

^{**} Corresponding author. Department of Electronic Engineering, National Kaohsiung University of Science and Technology, No. 415, Jiangong Rd., Sanmin Dist., Kaohsiung City, 80778, Taiwan, ROC.

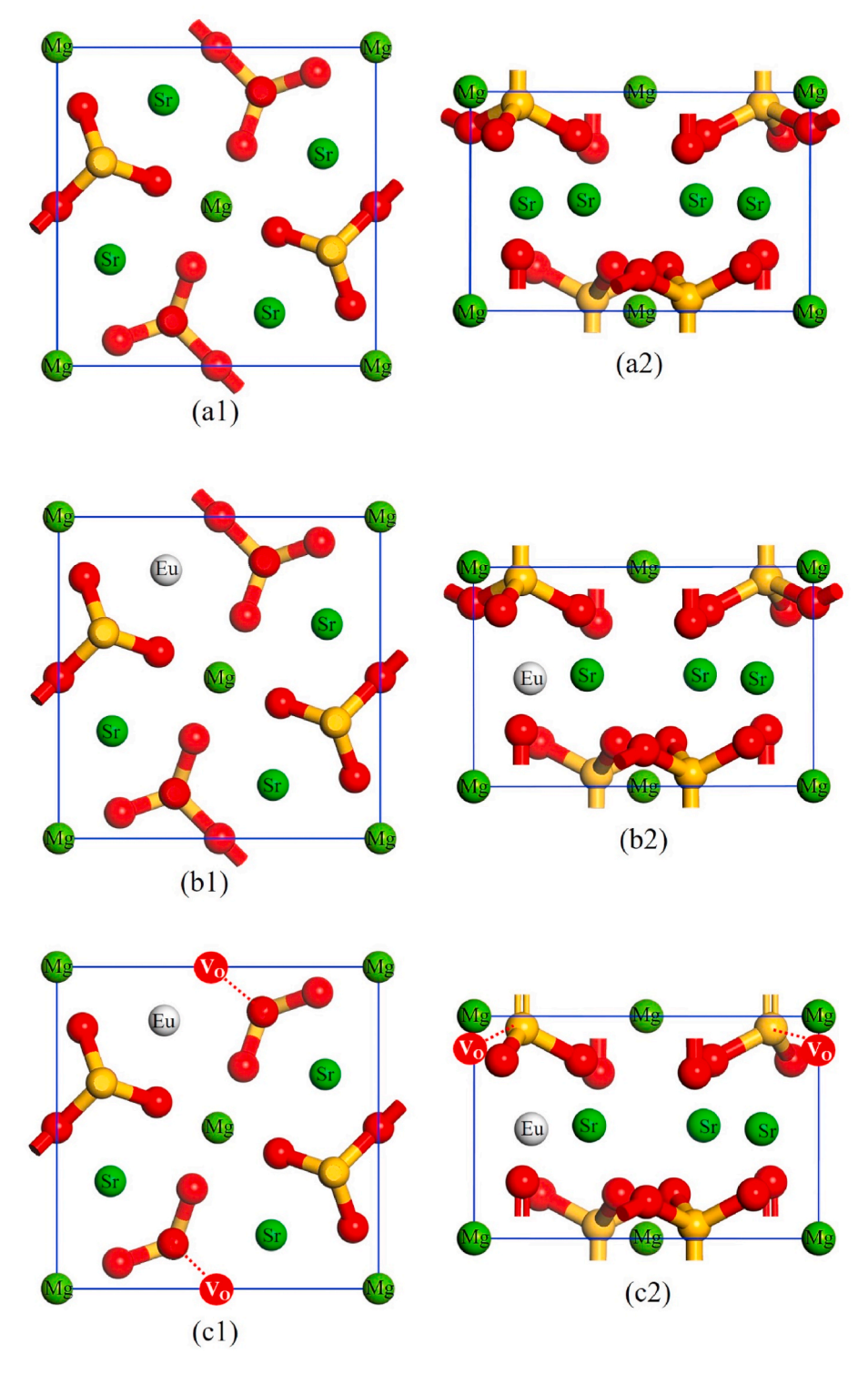


Fig. 1. Top (a1) and side (a2) views of the calculated model $Sr_4Mg_2Si_4O_{14}$ of host $Sr_2MgSi_2O_7$, top (b1) and side (b2) views of the calculated model $1 Sr_3Mg_2Si_4O_{14}$: Eu^{2+} as well as top (c1) and side (c2) views of the calculated model $2 Sr_3Mg_2Si_4O_{13}$: $Eu^{2+}(V_O)$ of phosphor $Sr_2MgSi_2O_7$: Eu^{2+} . Top (a'1, b'1, c'1) and side (a'2, b'2, c'2) views of the calculated geometry optimization results of $Sr_4Mg_2Si_4O_{14}$, $Sr_3Mg_2Si_4O_{14}$: Eu^{2+} (model 1) and $Sr_3Mg_2Si_4O_{13}$: $Eu^{2+}(V_O)$ (model 2), respectively.

In addition, the crystal phases and structures of these synthesized phosphors were studied by X-ray wide-angle diffraction (XRD) and field emission scanning electron microscopy (FESEM). The photoluminescence excitation (PLE) and photoluminescence (PL) spectra of these phosphors were studied using a fluorescence spectrophotometer. The binding energies of each surface composition of this phosphor were determined by X-ray photoelectron spectroscopy (XPS). The loss of

weight during the synthesis period was studied by thermogravimetric analysis (TGA).

Owing to the advantages of $Sr_2MgSi_2O_7$: Eu^{2+} blue phosphor powder such as low cost, ease of synthesis, lack of human toxicity, and environment friendliness, we try to explore the possibility and feasibility of its application to LFP discovery. For this, the pattern identification of LFPs on the surfaces of various materials is evaluated.

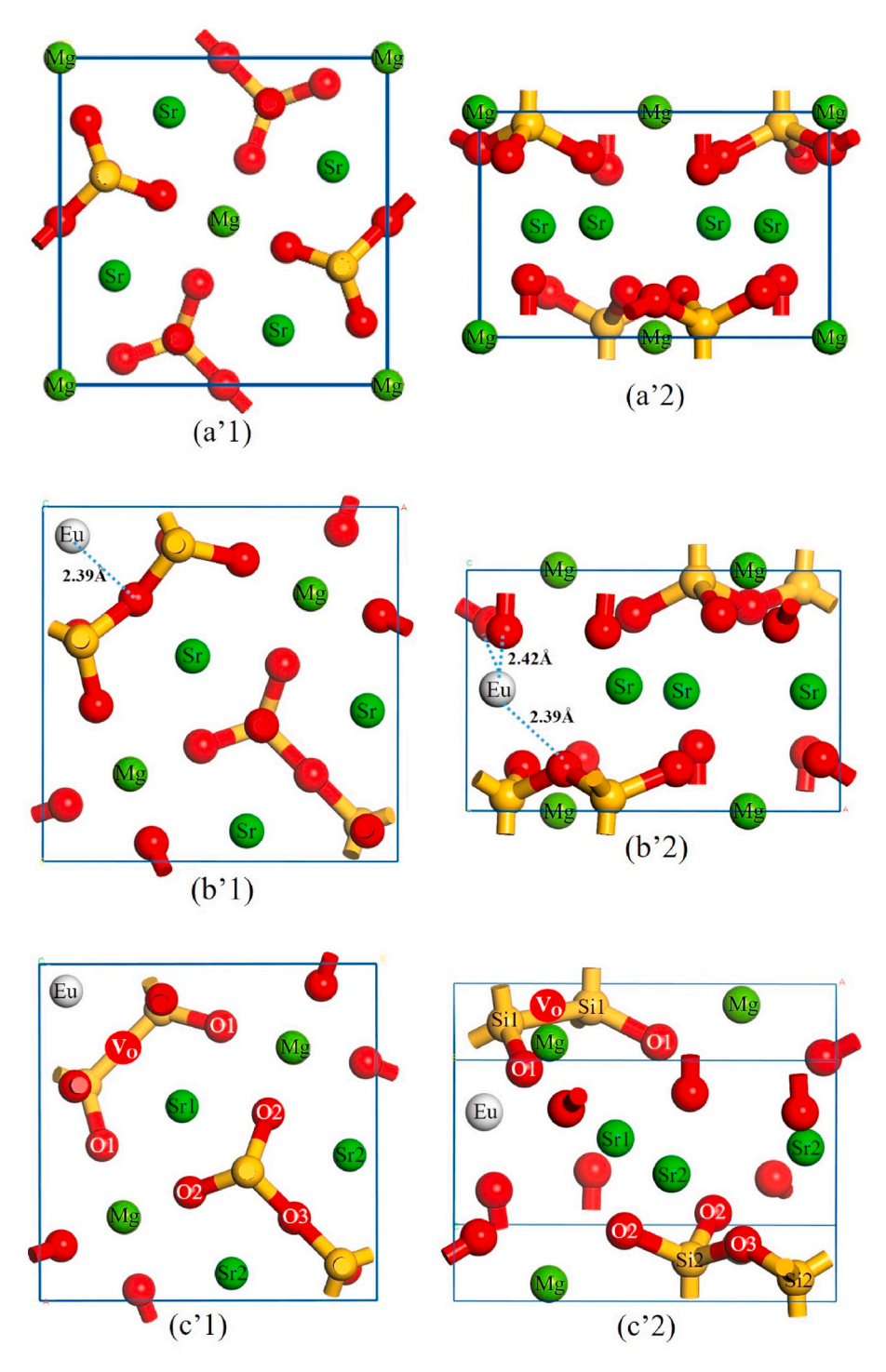


Fig. 1. (continued).

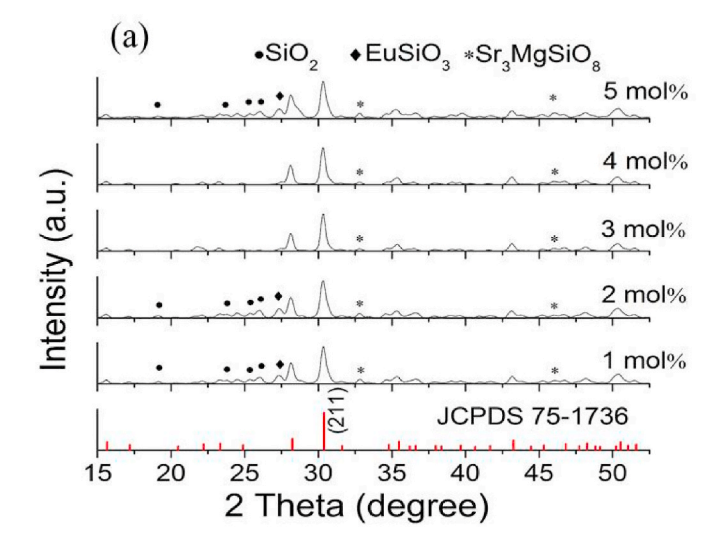
2. Experimental section

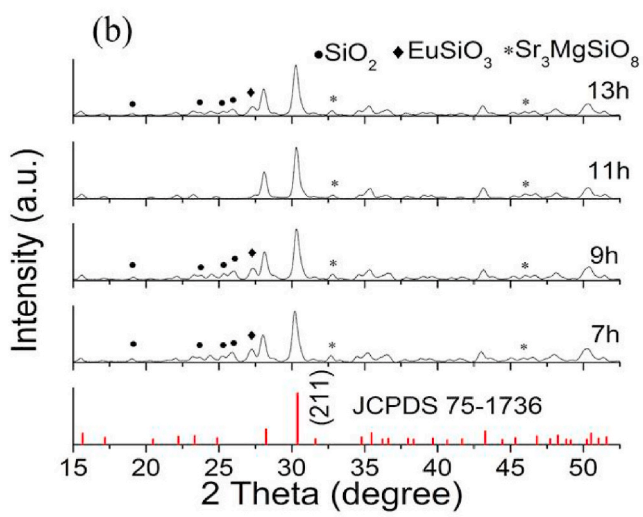
2.1. Powder synthesis

 $Sr_2MgSi_2O_7$: $xEu^{2+}~(x=0.01,0.02,0.03,0.04,0.05)$ phosphors were synthesized using a co-precipitation method. Magnesium nitrate hexahydrate (Mg(NO_3)_2 \cdot 6H_2O, 99+%, Acros Organics, Belgium), strontium nitrate (Sr(NO_3)_2, 99+%, Acros Organics, Belgium), europium(III) acetate hydrate (Eu(C_2H_3O_2)_3 \cdot xH_2O, 99.9%, REacton, Alfa Aesar, U.S.A.), tetraethyl orthosilicate (Si(OC_2H_5)_4, 98%, Acros Organics, Belgium), deionized water, anhydrous alcohol (C_2H_5OH, 99.5+%, ECHO Chemical

Co., Ltd, Taiwan), and ammonium hydroxide (NH_4OH , 28–30%, Fisher Chemical, U.S.A.) were used as the starting materials.

First, stoichiometric amounts of Mg(NO₃)₂•6H₂O, Sr(NO₃)₂, and Eu (C₂H₃O₂)₃·xH₂O were placed in a beaker, and deionized water was added. These materials were heated and stirred at 300 rpm for 30 min at a temperature of 60 °C (so that they were evenly dissolved) to form solution A. A stoichiometric amount of Si(OC₂H₅)₄ was fully dissolved in anhydrous alcohol and stirred for 30 min to form solution B. Then, solution B was poured into solution A, and the mixture was heated and stirred at 300 rpm for 30 min at a temperature of 60 °C to obtain a uniformly mixed solution C. Subsequently, ammonium hydroxide was





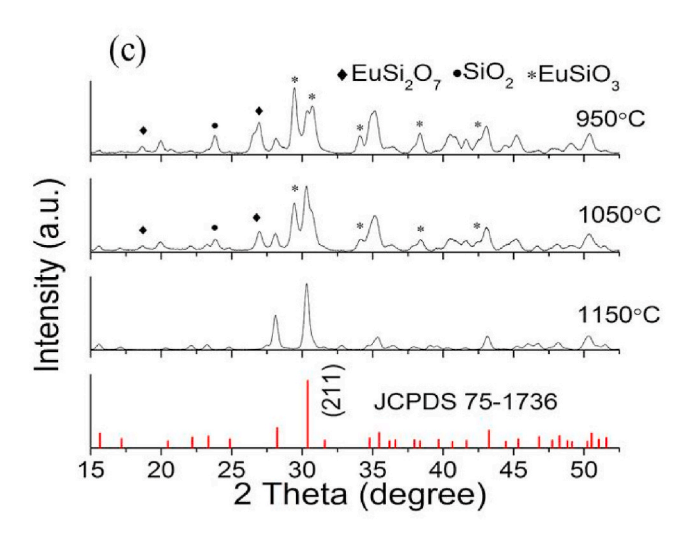


Fig. 2. XRD patterns of (a) $Sr_2MgSi_2O_7$: xEu^{2+} ($x=0.01,\ 0.02,\ 0.03,\ 0.04,\ 0.05$) (b) $Sr_2MgSi_2O_7$: $4mol\%\ Eu^{2+}$ phosphor sintered from 7 to 13 h at 1150 °C (c) $Sr_2MgSi_2O_7$: $4mol\%\ Eu^{2+}$ phosphor sintered from 950 to 1150 °C as compared to the standard pattern, respectively.

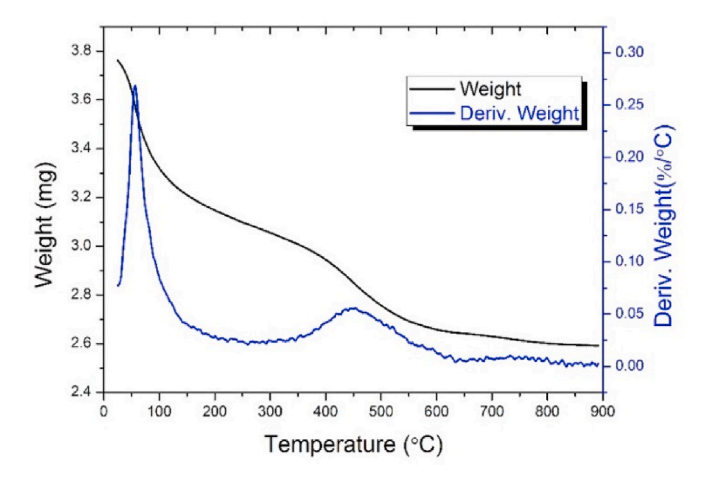


Fig. 3. DTA-TGA analysis of precursors after co-precipitation of $Sr_2MgSi_2O_7$: $4mol\%Eu^{2+}$.

dropped into solution C until the solution was completely turbid (white color). It was poured into a plastic test tube and centrifuged at 6000 rpm for 30 min to obtain a white solid.

The obtained white solid was washed with deionized water and anhydrous alcohol and then baked at 80 °C for 20 h to remove excess water. The white precursor was ground in a mortar, after which it was placed in a crucible and sintered in a high-temperature furnace. After final grinding of the resulting product, bright blue phosphor powder was obtained. A series of $Sr_2MgSi_2O_7$: xEu^2 + phosphors doped with 1, 2, 3, 4, and 5 mol% Eu^2 + were sintered at 1150 °C for 11 h. The optimum doped $Sr_2MgSi_2O_7$: 4 mol% Eu^2 + phosphor was sintered at 950, 1050, and 1150 °C for 11 h as well as for 7, 9, 11, and 13 h at 1150 °C.

2.2. Characterization

The crystal structures of the synthesized phosphors were recorded on a 2D high-temperature D8 Discover (Bruker AXS Gmbh, Karlsruhe, Germany) X-ray wide-angle diffractometer (XRD) with Cu $k\alpha_{1+2}$ = 1.54184 Å radiation at 40 kV and 40 mA. Their particle size was analyzed using a nanoparticle analyzer (HORIBA Scientific SZ-100Z). The morphology was observed by field emission scanning electron microscopy (FESEM) (JEOL-6330). The photoluminescence (PL) and photoluminescence excitation (PLE) spectra as well as their decay time of phosphors were examined at room temperature using a fluorescence spectrophotometer (Hitachi Fluorescence Spectrophotometer F-7000) having a 150 W Xe lamp as an excitation source. The CIE color coordinates of the prepared phosphor were calculated by radiation spectroscopy. X-ray photoelectron spectroscopy (XPS) was performed to determine the binding energy of each component element (JEOL, JAMP-9500F Auger Electron Spectroscopy). Thermogravimetric analysis (TGA) and differential thermal analysis (DTA) were performed in air using a TA SDT 2960 system having a heating rate of 10 °C/min from 25 °C to 900 °C.

2.3. Computational details

In addition to the host model of SMSO, the Eu^{2+} - doped model (model 1) and the model with extra oxygen vacancy (model 2) were built based on the primitive $Sr_4Mg_2Si_4O_{14}$ crystal cell shown in Fig. 1 (a1–c2). The calculated models (model 1 and model 2) were expressed as $Sr_3Mg_2Si_4O_{14}$: Eu^{2+} and $Sr_3Mg_2Si_4O_{13}$: $Eu^{2+}(V_O)$, respectively. In model 1, one Sr atom was replaced by one Eu^{2+} ion in the primitive crystal cell to study the Eu^{2+} ion-doping effect. In calculated model 2 also, one Sr atom was replaced by one Eu^{2+} ion in the primitive crystal cell. Simultaneously, the oxygen atom between two Si atoms in the Si_2O_7

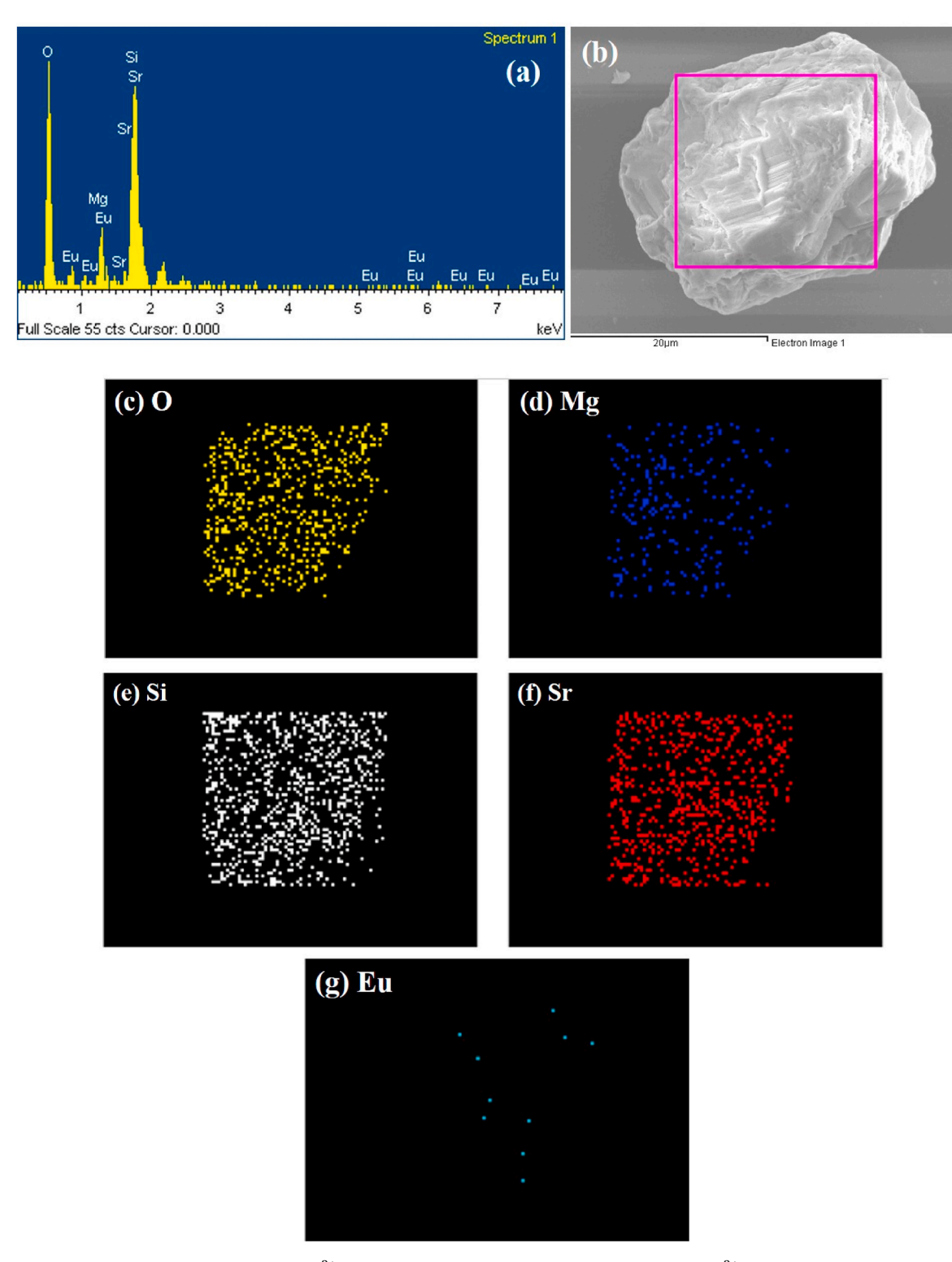


Fig. 4. (a) EDS analysis chart of $Sr_2MgSi_2O_7$: 4 mol% Eu^{2+} (b) the range of EDS analysis in $Sr_2MgSi_2O_7$: 4 mol% Eu^{2+} particle, (c \sim g) O, Mg, Si, Sr and Eu element mark of EDS analysis, respectively.

skeleton near the Eu^{2+} doping ion was removed to understand the oxygen vacancy effect.

The geometry optimization task of the band structures and partial density of states (PDOS) of the calculated host model, model 1, and model 2 were performed using the CASTEP program [54–59] with the generalized gradient approximation (GGA) based on the Perdew–Burke–Ernzerhof (PBE) formulation. The charges of these models had to be modified to +1 to ensure normal execution of the calculation

tasks. The kinetic cutoff energy was 340.0 eV for the host model and 430.0 eV for both model 1 and model 2. The k-point sampling scheme of a 3 \times 3 \times 5 Monkhorst–Pack grid and ultrasoft pseudopotential were used for the primitive cell.

The top and side views of the host model of SMSO are shown in Fig. 1 (a1) and (a2), respectively. The top and side views of model 1 with an Eu^{2+} doping ion are shown in Fig. 1(b1) and (b2), respectively. The top and side views of model 2, which includes one oxygen vacancy near the

 $\begin{tabular}{lll} \textbf{Table 1} \\ \textbf{Weight, atomic percentage and theoretical value of each element of Sr2MgSi2O7:4mol%Eu2+.} \\ \end{tabular}$

Element	Weight%	Atomic%	Theoretical Atomic%
Sr	54.16	21.70	16.33
Mg	6.45	9.31	8.33
Si	16.23	20.28	16.67
O	22.09	48.46	58.33
Eu	1.08	0.25	0.33

 Eu^{2+} doping ion are shown in Fig. 1(c1) and (c2), respectively. For convenience of comparison, the calculated geometry optimization results are shown at the bottom of Fig. 1. The top and side views of the calculated results for the host crystal model, doped model 1, and doped model 2 are shown in Fig. 1 (a'1 – c'2).

3. Results and discussion

The X-ray diffraction (XRD) patterns of $Sr_2MgSi_2O_7$: xEu^{2+} (x = 0.01, 0.02, 0.03, 0.04, and 0.05) sintered at 1150 °C for 11 h are shown in Fig. 2(a). The measured results are roughly consistent with the standard card JCPDS 75-1736 of Sr₂MgSi₂O₇. All these have a tetragonal crystal structure. As the concentration of Eu²⁺ ions increases, the distance between Eu²⁺ ions narrows, and the probability of energy transfer among Eu²⁺ ions increases. Therefore, the concentration of Eu²⁺ doping ions must be appropriate to avoid the effect of concentration quenching. When the doping concentration is increased to 4 mol%, the Eu²⁺ ions can be better incorporated into the host, resulting in fewer impurities such as Sr₃MgSiO₈, EuSiO₃, and SiO₂. The main peak is located at 30.40°, with the major phase characterized by the (211) plane. Its full width at half maximum (FWHM) was analyzed, and the results showed that the FWHM decreases gradually with an increase in concentration until 4 mol%. This indicates that the best crystallinity of the phosphor powder is at 4 mol%.

The XRD patterns of $Sr_2MgSi_2O_7$: 4 mol% Eu^{2+} phosphors sintered for 7, 9, 11, and 13 h at 1150 °C, as well as those sintered at 950, 1050, and 1150 °C for 11 h are shown in Fig. 2(b) and (c). The results agree with the peak position shown in JCPDS 75–1736 for $Sr_2MgSi_2O_7$, which has a tetragonal crystal structure. Only a small amount of Sr_3MgSiO_8 impurity was present in the sample sintered for 11 h. With a decrease in the sintering temperature, the peaks of impurities such as $Eu_2Si_2O_7$, $EuSiO_3$, $EuSi_2O_7$, and SiO_2 appeared in the XRD pattern. The minimum FWHM values for the samples sintered for 11 h at 1150 °C indicate that the samples achieved the best crystallinity under these conditions. When the sintering temperature was higher than 1150 °C, the samples adhered to the crucible to form a bulk and could not form a powder.

The phosphor sintered at 1150 °C had a significantly narrower peak than those sintered at other temperatures, and no other impurities were produced. With a decrease in the sintering temperature, the main peak combined with the peaks of other impurities. This blue phosphor possessed the best crystallinity at 1150 °C. The small amount of $\rm Eu^{2+}$ doping ions that was applied to the phosphor samples did not have any influence on the phase of the phosphors. From the above results, it can be seen that a higher doping concentration and longer sintering time will produce more impurities.

Fig. 3 shows the $Sr_2MgSi_2O_7$: $4mol\%Eu^{2+}$ precursor subjected to DTA-TGA after precipitation. The weight loss is understood to be caused due to the increase in temperature during the sintering process. From this figure, the reaction process and the minimum temperature required to produce the final product can be inferred. When the temperature rises to $56\,^{\circ}C$ and $450\,^{\circ}C$, the precursor loses weight significantly. The former can be attributed to the loss of the organic solvent and evaporation of absorbed moisture from the material. The latter is caused by the synthetic reaction of $SrSiO_3$ and SiO_2 as well as the removal of excess impurities. According to the results of X-ray diffraction, this blue phosphor

needs to be synthesized at a higher temperature.

From the SEM images, it can be seen that there were no significant changes in the particle size and appearance of the phosphor powder regardless of the sintering time and temperature. The particle size was approximately 4 μm and the crystal structure was tetragonal. To confirm that the Eu²+ ion was indeed doped into the Sr2MgSi2O7 host, we performed energy dispersive spectrometry (EDS) analysis to understand the composition ratio of the elements.

The results of EDS analysis of $Sr_2MgSi_2O_7$: 4 mol% Eu^{2+} are shown in Fig. 4(a). Fig. 4(b) shows the range of the EDS analysis performed on the $Sr_2MgSi_2O_7$: 4 mol% Eu^{2+} particles. Fig. 4(c–g) show the O, Mg, Si, Sr, and Eu element distributions in the particle, respectively. From the results shown in Fig. 4, the existence of each element of the host $Sr_2MgSi_2O_7$ and the presence of the doped ion Eu^{2+} can be observed. These elements and Eu^{2+} ions are distributed evenly in the particle. Fig. S2 shows the SEM images for various sintering times (from 7 to 13 h in a1–a4), sintering temperatures (from 950 to 1150 °C in b1–b3), and various doping concentrations of Eu^{2+} (from 1 to 5 mol in c1–c5).

The weight and atomic percentages of each element are listed in Table 1. Except for O and Eu, the contents of Mg, Si, and Sr are higher than the theoretical values. The weight and atomic percentages of the doped ion and the host material generally agree with the theoretical values. The particle size of the phosphor is roughly distributed in the range of 3–5 μm , and the average particle size is approximately 4 μm (the particle size analysis chart of Sr₂MgSi₂O₇: 4 mol% Eu²⁺ is shown in Fig. S1). According to this result, the particle size of the phosphor powder should correspond with the requirement of a latent fingerprint application.

Fig. 5(a) shows the full-scan X-ray photoelectron spectroscopy (XPS) analysis of $Sr_2MgSi_2O_7$: 4 mol% Eu^{2+} , and the presence of all the elements in the $Sr_2MgSi_2O_7$: 4 mol% Eu^{2+} sample can be observed in this figure. The C 1s peak at 285 eV was used to calibrate the energy scale of the other elements. The binding energies of Si 2p and Sr 3d core electrons can be observed near 100 eV and 133 eV, respectively. The binding energies of the 1s electrons of O and Mg are approximately 534 eV and 1305 eV, respectively. The signals of all the elements can be clearly seen in Fig. 5(b)–5(e).

Owing to rigidity of the tetragonal structure of the $\rm Si_2O_7$ frame, the shapes of the binding energies of Si and O are clearly visible. There is a small signal at 105 eV, as shown in Fig. 5(c), which can be attributed to the signal caused by $\rm SiO_2$. Mg and Sr ions are flexible in the phosphor, and hence their XPS shapes are unstable. Because the concentration of doped Eu ions is very low, the noise is too high to identify the complete signal. The binding energies of Eu are very small and are estimated to be about 1125 and 1155 eV (Fig. S3). The binding energies assigned to Eu $\rm 3d_{3/2}$ and Eu $\rm 3d_{5/2}$ are usually located at about 1167.3 and 1136.4 eV, which indicate that the valence state of Eu is +3 [60]. In the XPS of Eu ions, the peaks of the binding energies located at about 1155.7 and 1125.3 eV originate from the $\rm Eu^{2+}$ $\rm 3d_{3/2}$ and $\rm 3d_{5/2}$ levels, respectively [61]. This indicates that the bright blue-emitting light of this phosphor radiates from the $\rm Eu^{2+}$ ions instead of $\rm Eu^{3+}$ ions.

Fig. 6(a) and (b) show the excitation PLE and emission PL spectra of the $Sr_2MgSi_2O_7$: xEu^{2+} phosphors sintered at 1150 °C for 11 h with various sintering concentrations of 1, 2, 3, 4, and 5 mol%. The PLE and PL spectra of $Sr_2MgSi_2O_7$: 4 mol% Eu^{2+} at various sintering temperatures from 950 to 1150 °C are shown in Figs. S4(a) and (b). The phosphor was excited by NUV light at 337 nm and monitored at 486 nm in the PLE spectra. The excitation band is attributed to the 4 $F^7 \rightarrow 4F^65D^1$ transition of the Eu^{2+} ion. The phosphor powder excited at 337 nm also emits blue light at 486 nm due to the electronic transition of $4F^65D^1$ to $4F^7$. When the doping concentration of $4F^65D^1$ to $4F^7$. When the doping concentration of $4F^7$ was more than 4 mol%, the amount of activator was very high, and the energy transfer between ions became frequent. The conversion efficiency of the radiant energy was reduced, resulting in a decrease in the luminous efficiency. Thus, the effect of concentration quenching caused a reduction in the luminescence intensity.

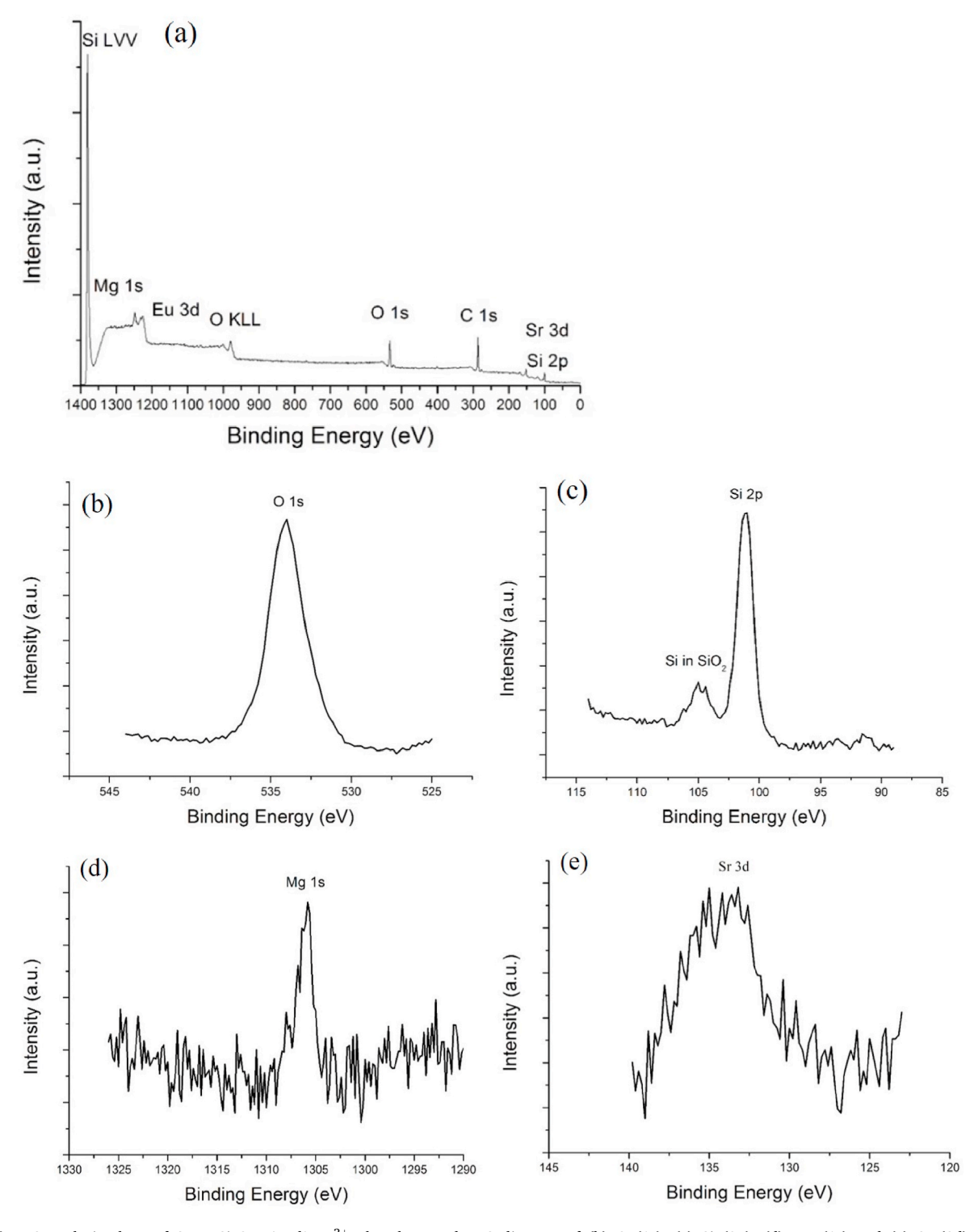


Fig. 5. (a) XPS analysis chart of $Sr_2MgSi_2O_7$: $4mol\%Eu^{2+}$ phosphor; and XPS diagram of (b) O (1s), (c) Si (2p), (d) Mg (1s) and (e) Sr (3d) orbitals in $Sr_2MgSi_2O_7$: $4mol\%Eu^{2+}$ phosphor.

The shapes of the PLE and PL spectra of the $Sr_2MgSi_2O_7$: 4 mol% Eu^{2+} phosphors sintered at 1150 °C for various sintering times (7, 9, 11, and 13 h) did not change significantly. When the sintering temperature was lowered from 1150 to 1050 °C, the radiation intensity was significantly reduced, and there was almost no radiation in the PL spectrum at 950 °C. This means that the optimum sintering temperature for the phosphor powder $Sr_2MgSi_2O_7$: 4 mol% Eu^{2+} is approximately 1150 °C. If the crystal field is stronger, the degeneracy of the energy levels splits

further, which will cause a red shift in the band.

The decay curves of the $Sr_2MgSi_2O_7$: xEu^{2+} (x=0.01, 0.02, 0.03, 0.04, 0.05) phosphors and the influence of Eu^{2+} concentration on the lifetime are shown in Fig. 6(c). The monitoring wavelength was 486 nm with an excitation at 337 nm. The fitting curves overlap with the experimental data to a first-order exponential decay equation. This means that this phosphor has only a single illumination mechanism. When the concentration of doping ions increases, the non-radiative

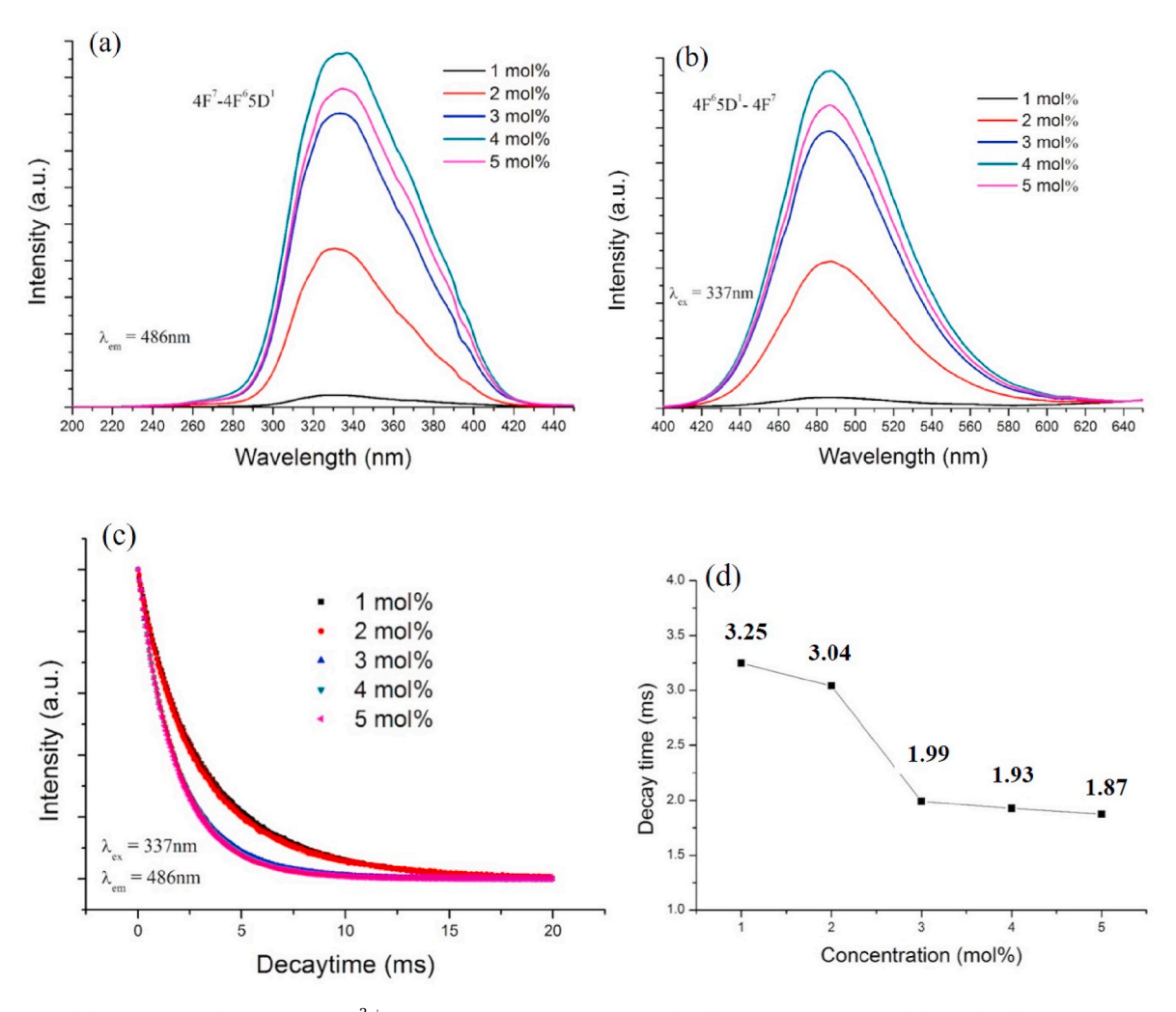


Fig. 6. (a) PLE and (b) PL spectra of $Sr_2MgSi_2O_7$: xEu^2 +(x = 0.01, 0.02, 0.03, 0.04, 0.05) phosphors. (c) Decay curves of these phosphors at room temperature. (d) The influence of Eu^2 concentration to its lifetime (unit = ms).

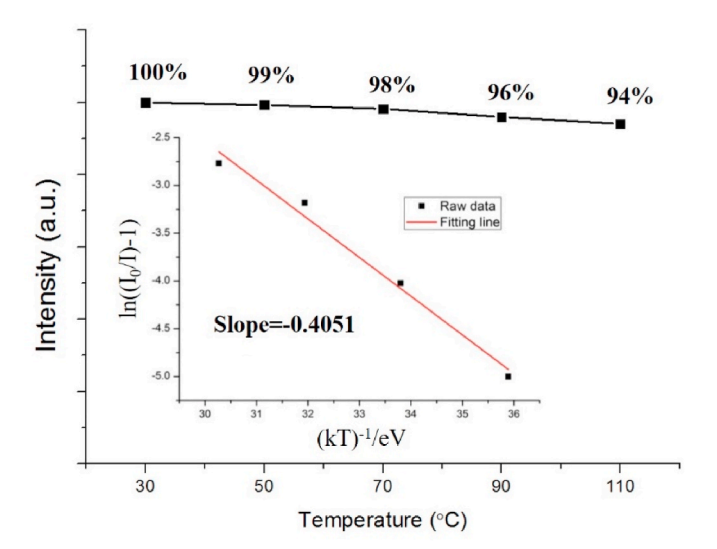


Fig. 7. Remaining luminous intensity at various temperatures from 30 to 110 $^{\circ}\text{C}$ of $Sr_2MgSi_2O_7$: $4mol\%Eu^{2+}$ phosphor. Inset: The diagram of calculated activation energy of $Sr_2MgSi_2O_7$: $4mol\%Eu^{2+}$ phosphor.

CIE color coordinates of Sr2MgSi2O7: xEu2+ (x = 0.01, 0.02, 0.03, 0.04, 0.05).

Concentration(mol%)	CIE X	CIE Y
1%	0.1871	0.6181
2%	0.1780	0.6286
3%	0.1791	0.6350
4%	0.1755	0.6366
5%	0.1800	0.6347

energy conversion between ions also increases, resulting in a decrease in the decay time. The decay times obtained by fitting the concentrations of 1–5 mol% are 3.25, 3.04, 1.99, 1.93, and 1.87 ms, as shown in Fig. 6(d). The decay time of the obtained phosphor decreases gradually as the doping concentration increases. The measured external quantum efficiency of this blue phosphor is approximately 30%. Because of the blue emission band, it can be excited by a near-UV excitation source of at least 310–380 nm. Thus, the blue phosphor obtained in our work matches the excitation wavelength of the NUV LED chip.

The $Sr_2MgSi_2O_7$: 4 mol%Eu²⁺ phosphor powder with the strongest radiation intensity was heated to various temperatures ranging from 30 °C to 110 °C and excited at 337 nm for PL analysis. The luminous intensity at each temperature is plotted in Fig. 7. The intensity decay curve of this phosphor is almost linear. When this phosphor is heated to 110 °C, the remaining intensity is approximately 94% of the original luminous intensity.

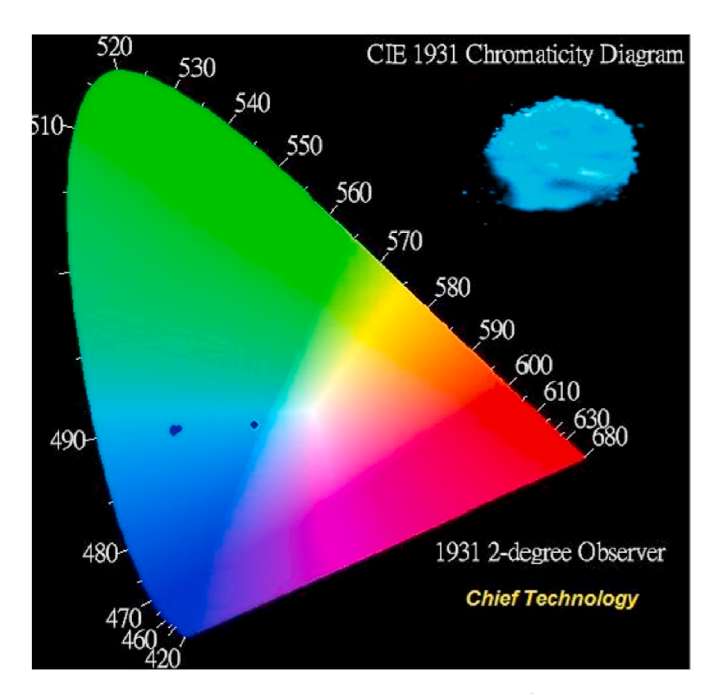


Fig. 8. The CIE chromaticity diagram of $Sr_2MgSi_2O_7$: xEu^{2+} (x=0.01, 0.02, 0.03, 0.04, 0.05) phosphors at 337 nm excitation. Inset shows the photographs of $Sr_2MgSi_2O_7$: 4mol% Eu^{2+} under the UV lamp.

The probability of the thermal quenching process is dependent on the activation energy. The activation energy of the $Sr_2MgSi_2O_7$: 4 mol% Eu^{2+} phosphor was calculated using the Arrhenius equation to explore the thermal stability and is shown in the inset of Fig. 6. The calculated activation energy of this phosphor was 0.4051 eV. This proves that this phosphor has an extremely high thermal stability. The high anti-thermal quenching property could be due to the rigid network of silicate (Si_2O_7) layers in its crystal structure. The activation energy of this phosphor is between those of silicate based orange-red $SrSiO_3$: Eu^{3+} and bluish-green $BaSi_2O_2N_2$: Eu^{2+} phosphors, whose activation energies are about 0.94 eV [62] and 0.305 eV [63], respectively. This shows that the host $Sr_2MgSi_2O_7$ is superior and possesses significant potential for application in LED lighting.

Based on the calculation of the PL spectrum, the CIE color coordinates of each $Sr_2MgSi_2O_7$: xEu^{2+} sample are listed in Table 2. The CIE color coordinates of the optimally doped $Sr_2MgSi_2O_7$: 4 mol% Eu^{2+} phosphor are (0.1755, 0.6366). These coordinates are shown in the CIE chromaticity color coordinates in Fig. 8. The coordinates of these

phosphors are located in the bright blue area, except for the 1 mol% sample, which is close to the white light area. The CIE color coordinates are stable and do not change significantly with increase in doping concentration. It is almost impossible to change the color by modifying the concentration of doping ions. The inset shows that the $Sr_2MgSi_2O_7$: 4 mol% Eu^{2+} phosphor powder is excited by ultraviolet light in a dark room and emits blue light. The luminous intensity of the $Sr_2MgSi_2O_7$: 1 mol% Eu^{2+} phosphor is very low; hence, its measured CIE coordinate could be from the environmental light.

The basic structural units of SMSO crystals are composed of [SiO₄] tetrahedron, [MgO₄] tetrahedron, and [SrO₈] polyhedron, and its framework, which consists of a [Mg(Si₂O₇)] island group formed by corner-sharing of [SiO₄] tetrahedral with an inserted Mg atom, is well known [64]. From Fig. 1(a'1) and (a'2), it can be seen that the calculated results of host geometry optimization are almost the same as the initial construction. The calculated results of geometry optimization with doped Eu²⁺ ions (model 1) are shifted from the initial construction are shown in Fig. 1(b'1) and (b'2). The Eu²⁺ doping ion causes distortion in the crystal lattice and the shift of the Si₂O₇ skeleton. The bridging oxvgen connected two SiO₄ tetrahedra linked to the Eu²⁺ doping ion, forming a linkage with a distance of 2.39 Å (the shortest distance) on one side and two linkages with a distance of 2.42 Å on the other side. At these distances, a coordinate covalent bond could be formed by the Eu²⁺ doping ion with its neighboring oxygen atoms. This caused the Sr atoms to shift from the crystal lattice.

The role of oxygen vacancies as the electron trap center in this Sr₂MgSi₂O₇: Eu²⁺ phosphor has been identified in Ref. [65]. An oxygen vacancy labeled as Vo was created by removing the bridging oxygen connected to two SiO₄ tetrahedra to study the effect of oxygen vacancies. The Eu²⁺ doping ion and the oxygen vacancy V_O caused a distortion in the crystal lattice, and the Si₂O₇ skeleton shifted from the initial construction. The calculated results of geometry optimization on model 2 are shown in Fig. 1(c'1) and (c'2). The loss of the bridging oxygen atom causes the Si₂O₇ group to become Si₂O₆ group. The Si atom labeled as Si1 in the Si₂O₆ group is different from the Si atom labeled as Si2 in the Si₂O₇ group. The O atom labeled as O1 in the Si₂O₆ group is also different from the O atom labeled as O2 in the Si₂O₇ group. The bridging oxygen atom in the Si₂O₇ skeleton was labeled as O3. This oxygen vacancy causes the Sr atom to possess two different electronic structures; the Sr atom near V_O is labeled as Sr1 and the other is labeled as Sr2. The Eu^{2+} doping ion and the oxygen vacancy V_{O} cannot cause any change in the Mg atom.

The CASTEP band structure of the host model is shown in Fig. 9(a). The calculated band gap energy was 4.532 eV. Its valence band maximum (VBM) and conduction band minimum (CBM) are vertically

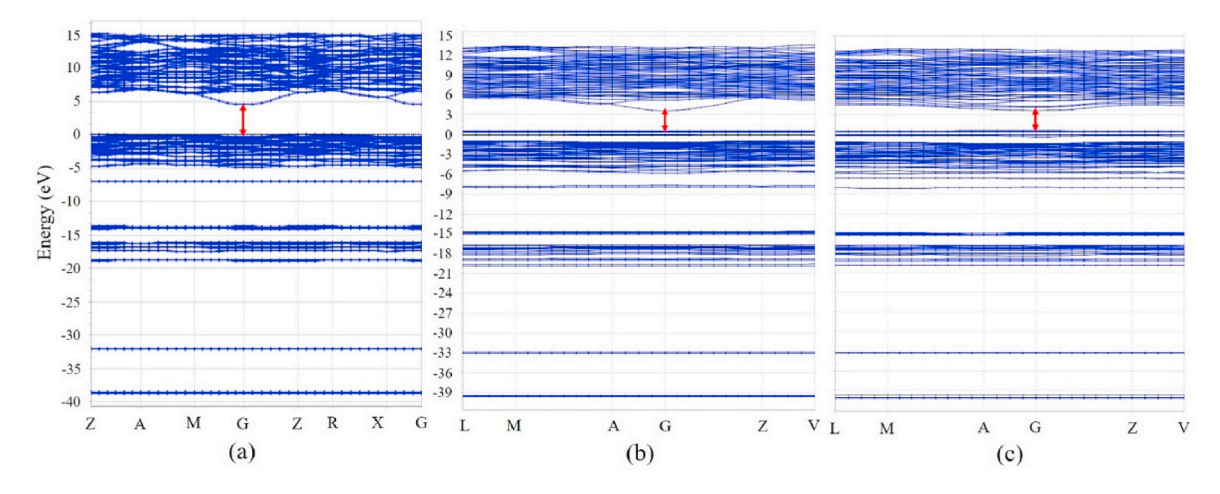


Fig. 9. The CASTEP band structure of (a) host model ($Sr_2MgSi_2O_7$) (b) doped Eu^{2+} ion model 1 ($Sr_3Mg_2Si_4O_{14}$: Eu^{2+}) (c) doped Eu^{2+} ion and oxygen vacancy V_O model 2 ($Sr_3Mg_2Si_4O_{13}$: Eu^{2+} (V_O)).

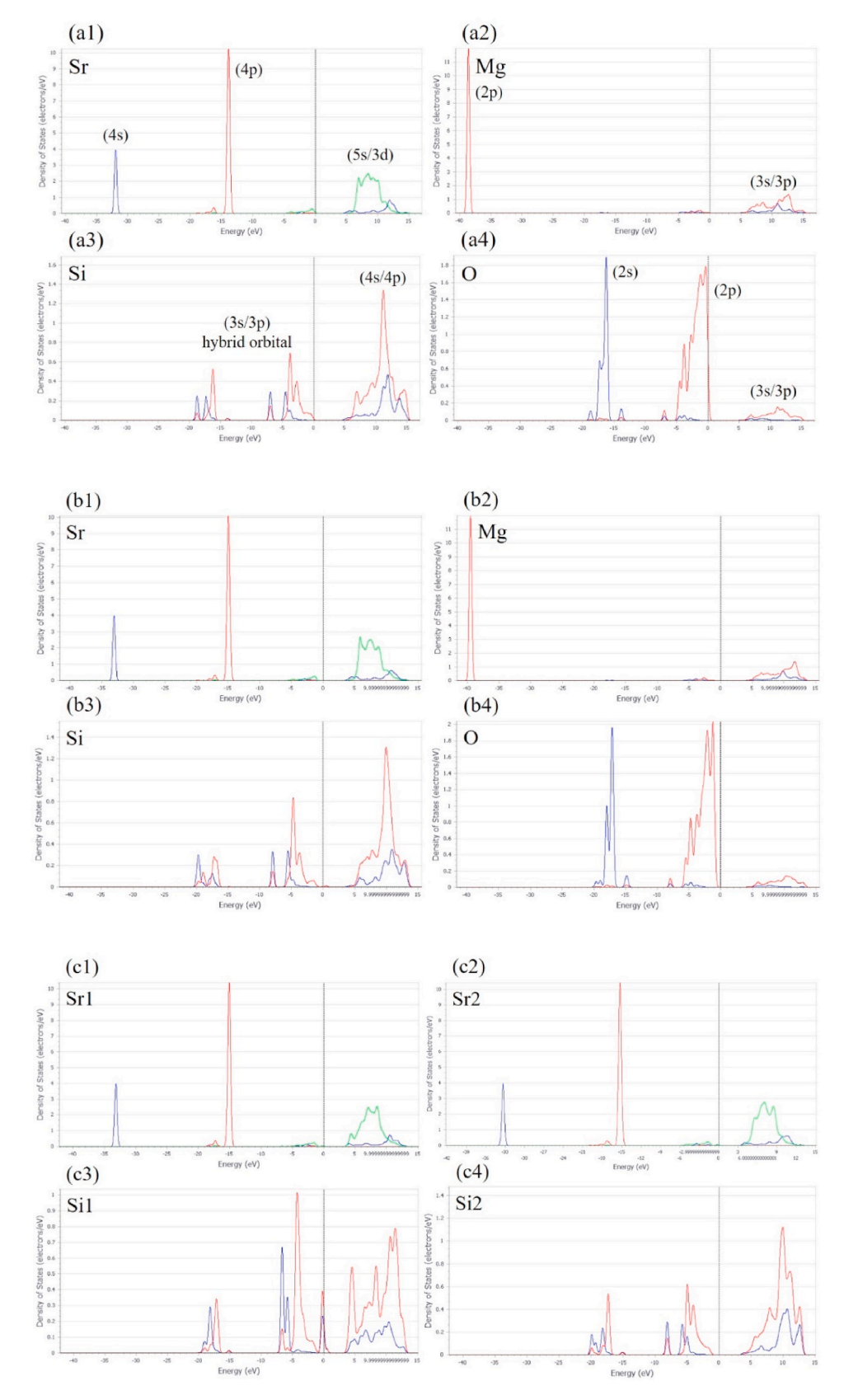


Fig. 10. The PDOS of (a1) Sr, (a2) Mg, (a3) Si, and (a4) O atoms in the calculated host model ($Sr_4Mg_2Si_4O_{14}$); (b1) Sr, (b2) Mg, (b3) Si, (b4) O and (b5) Eu components in the calculated model 1 ($Sr_3Mg_2Si_4O_{14}$: Eu^{2+}) as well as (c1) Sr1, (c2) Sr2, (c3) Si1, (c4) Si2, (c5) O1, (c6) O2, (c7) O3, (c8) Mg and (c9) Eu (V_O) components in the calculated model 2 ($Sr_3Mg_2Si_4O_{13}$: Eu^{2+} (V_O)).

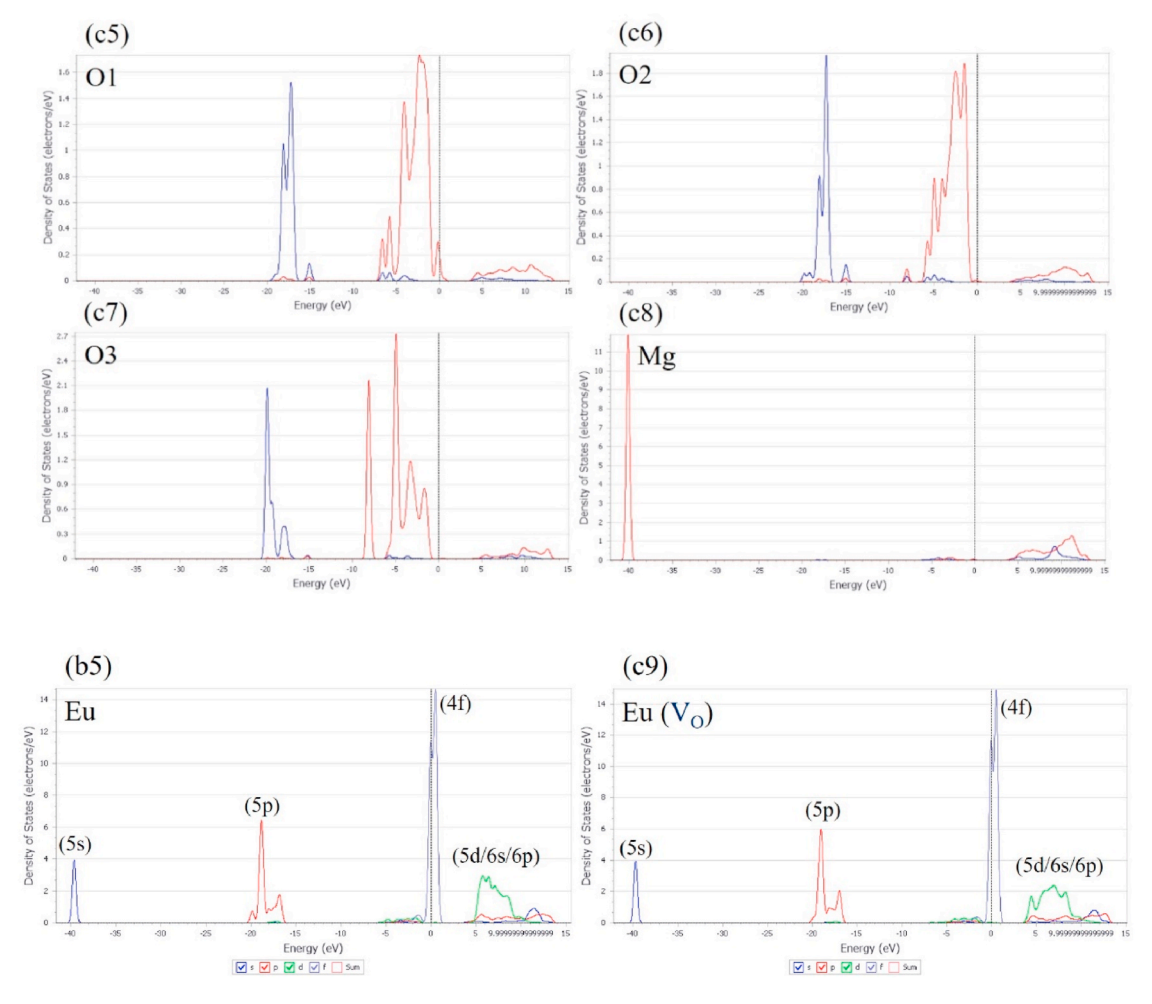


Fig. 10. (continued).

aligned, and the band gap is direct. The minimum band gap exists at the G point marked as a red line. The CASTEP band structures of the calculated models, namely model 1 and model 2, are shown in Fig. 9(a) and (b). Their calculated band gap energies are 0.396 and 0.452 eV, respectively. Because the calculated doped models are too simple compared to the real phosphor, the calculated band gap energies are not precise. However, their vertically aligned VBM and CBM, direct band gaps, and the minimum band gap existing at the G point can be consulted.

The calculated partial density of states (PDOS) of Sr, Mg, Si, and O atoms in the host model are shown in Fig. 10(a1-4). The PDOS of Sr, Mg, Si, and O atoms as well as Eu²⁺ ion in model 1 are presented in Fig. 10 (b1-5). The blue, red, green, and light blue curves represent the s, p, d, and f electron orbitals of each element. Although pseudopotential has been used throughout this work, there is another way to read out the principal quantum number of element atoms so that in PDOS plots, the usual labeling of the atomic shell can be applied. This involves finding the energy eigenvalue of atomic levels from the pseudopotential generating process, and then performing a single pseudo-atom calculation to match the valence orbital energy levels. The 4s, 4p, 5s, and 3d orbitals of the Sr atom are presented in Fig. 10(a1) and (b1). The 2p, 3s, and 3p orbitals of the Mg atom are presented in Fig. 10(a2) and (b2). The 3s/3p hybrid orbitals and the 4s and 4p electron orbitals of the Si atom are presented in Fig. 10(a3) and (b3). The 2s, 2p, 3s, and 3p orbitals of the O atom are presented in Fig. 10(a4) and (b4). When the Eu^{2+} ion replaces the Sr atom, there is no change in its s and p electron orbits; however, there is some change in the shape of the 3d empty orbit of the Sr atom. There is also no change in the s and p electron orbits of the Mg

atom. Eu $^{2+}$ doping has a significant effect on the s and p electron orbitals of Si and O atoms. Even the s and p electron orbitals in their inner layer are changed significantly. This means that the Eu $^{2+}$ ion forms a coordinate covalent bond with its adjacent O atom in the Si₂O₇ framework, which can also be proved from their distances of 2.39 Å and 2.42 Å.

The PDOS of Sr, Mg, Si, and O atoms as well as Eu²⁺ ion in model 2 are presented in Fig. 10(c1–9). The oxygen vacancy V_O causes changes in the orbitals of Si and O atoms; these changes also occur in the orbitals of Sr atoms. Therefore, we use two kinds of symbols to mark them, namely Sr1 and Sr2. It is interesting to note that there are no changes in the s and p orbits, but the 3d empty orbits have changed significantly. The 4s, 4p, 5s, and 3d orbitals of Sr1 and Sr2 atoms are presented in Fig. 10(c1) and (c2). Si1 and Si2 are the Si atoms that exist in the Si_2O_6 and Si_2O_7 skeletons, respectively. The 3s/3p hybrid orbitals and the 4s and 4p electron orbitals of the Si1 and Si2 atoms are presented in Fig. 10(c3) and (c4). From the above two figures, we can see that the shapes and values of the s and p orbits are different. This oxygen vacancy Vo causes the energy gap in the Si1 atom to decrease, and its parts of the s and p orbitals are even located on the Fermi surface. The oxygen vacancy Vo causes the electron orbitals of O atoms in the silicon skeleton to split into three kinds of O atoms: O1 to O3. The 2s, 2p, 3s, and 3p orbitals of O1, O2, and O3 atoms are presented in Fig. 10(c5), (c6), and (c7), respectively. Among them, O2 is the closest to the O atom in the original host, and the electron orbits of O1 and O3 have been changed significantly. The electron orbitals of the O3 atom move toward the inner layer, and the changes in the electron orbitals of the O1 atom are relatively small.

The 2p, 3s, and 3p orbitals of the Mg atom in model 2 are presented in Fig. 10(c8). The orbitals of the Mg atom at different positions look the

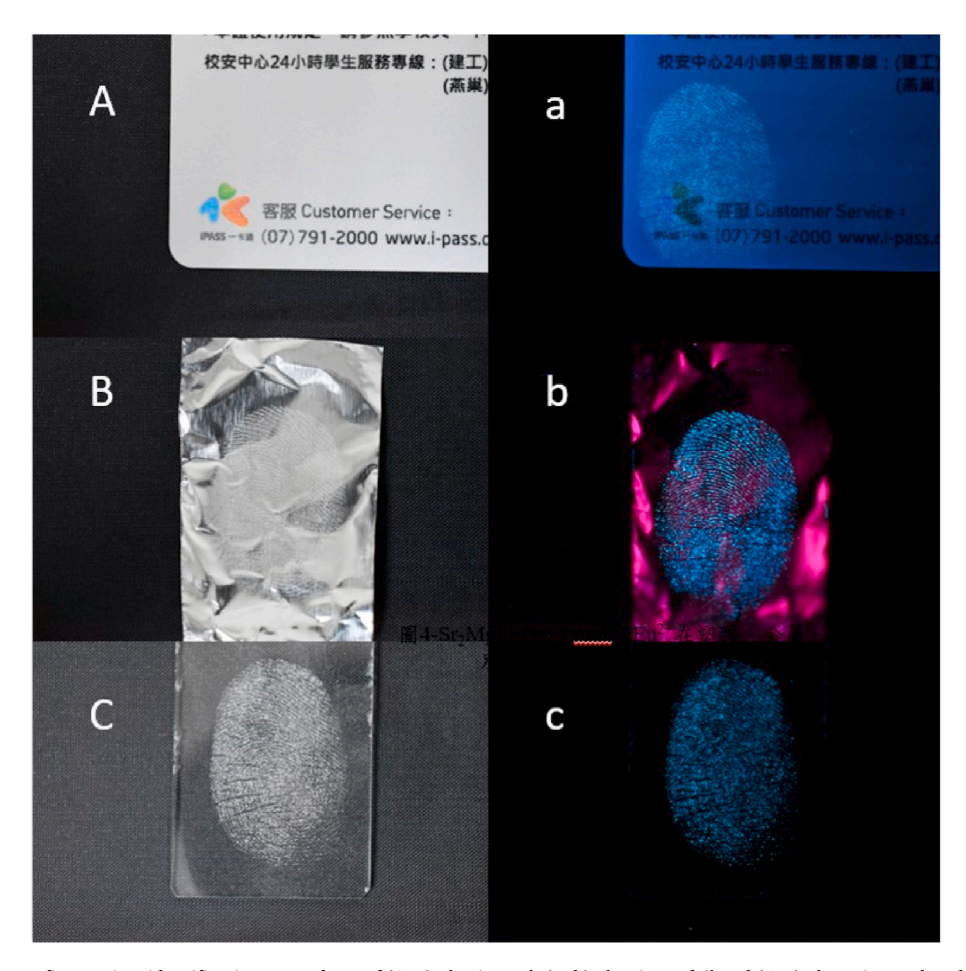


Fig. 11. The images of latent fingerprints identification on surfaces of (A, a) plastic card, (B, b) aluminum foil and (C, c) glass piece colored with $Sr_2MgSi_2O_7$: 4mol% Eu^{2+} phosphor in fluorescent lamp and UV light, respectively.

same, and the V_O has no effect on these orbitals. This is similar to the electron orbits of Mg atoms in the host. The 5s, 5p, 4f, 5d, 6s, and 6p electron orbitals of the Eu^{2+} ion in models 1 and 2 are shown in Fig. 10 (b5) and (c9). These two figures show that the oxygen vacancy V_O has no obvious effect on the s, p, and f orbitals of Eu^{2+} ions, but it has a significant effect on the 5d empty orbital. This means that there may be some electrons flowing into this 5d empty orbit.

The fingerprint is an important information for identifying a person, because it is a permanent record of each person. For this reason, the detection of fingerprints is an important process in forensic science. In particular, the confirmation of invisible latent fingerprints (LFPs) is a powerful evidence for the identification of suspects. Hence, many methods have been developed to discover LFPs, such as powder dusting [66], multi-metal deposition [67], superglue fuming [68], carbon dots [69], and fluorescent dyes [70]. Among them, the powder dusting method allows LFPs to be visualized within a short time and does not have any complicated requirements. However, traditional powder dusting methods have drawbacks such as low resolution, low sensitivity, low contrast, high background noise, and even toxicity [71,72]. Highly efficient luminescent materials with small particle sizes are potential solutions to overcome these weaknesses and to make LFPs more visible [73].

Fingerprints have interesting characteristics such as whorl, curve, and circle ridges that do not change with age. There are three levels of fingerprints. Level 1 provides pattern information such as the arches, loops, and whorls of LFPs. Level 2 describes the minutiae points including core, bifurcation, delta, bridge, enclosure, island, short ridge, and hook. Their random combinations result in the uniqueness and invariability of fingerprints. Level 3 refers to the shape, number, and

location of sweat pores, and although they alone cannot be used to detect LFPs, they provide reference information for partial defects or a blurry level 2 of LFPs [74–77]. Although this SMSO phosphor has been used in many products and fields, there has not been any research regarding the application of this phosphor to LFP recognition. Therefore, we try to understand the possibility of this application.

In Fig. 11, we can see the spreading of $Sr_2MgSi_2O_7$: 4 mol% Eu^{2+} phosphor on the surface of various materials and the identification of LFP. Fig. 11(A, a), (B, b), and (C, c) show LFP identification on the surfaces of a plastic card, aluminum foil, and glass piece, respectively, colored with this blue phosphor and viewed under a fluorescent lamp and UV light. They are all able to show the fingerprint patterns. Fig. 12 shows various features of the ridges and cracks of the marked fingerprint. The level 2 patterns of the eye, scar, bifurcation, island, delta, and terminate could emerge on the uneven surface of the aluminum foil. This indicates that this silicate-based blue phosphor has the potential to be used for the recognition of LFPs on irregular metallic surfaces. This SMSO phosphor powder is a strong candidate for the identification of LFPs on surfaces.

4. Conclusion

In this investigation, the blue phosphor powder $Sr_2MgSi_2O_7$: Eu^{2+} was successfully prepared using the co-precipitation method. According to our experimental results, the ideal condition for synthesizing the optimum doped concentration of $Sr_2MgSi_2O_7$: $4mol\%\ Eu^{2+}$ phosphor is sintering at 1150 °C for 11 h. The luminescence characteristics of XRD, PLE/PL, and XPS as well as the decay time, CIE color coordinates, and thermal stability of this phosphor were studied. Its external quantum

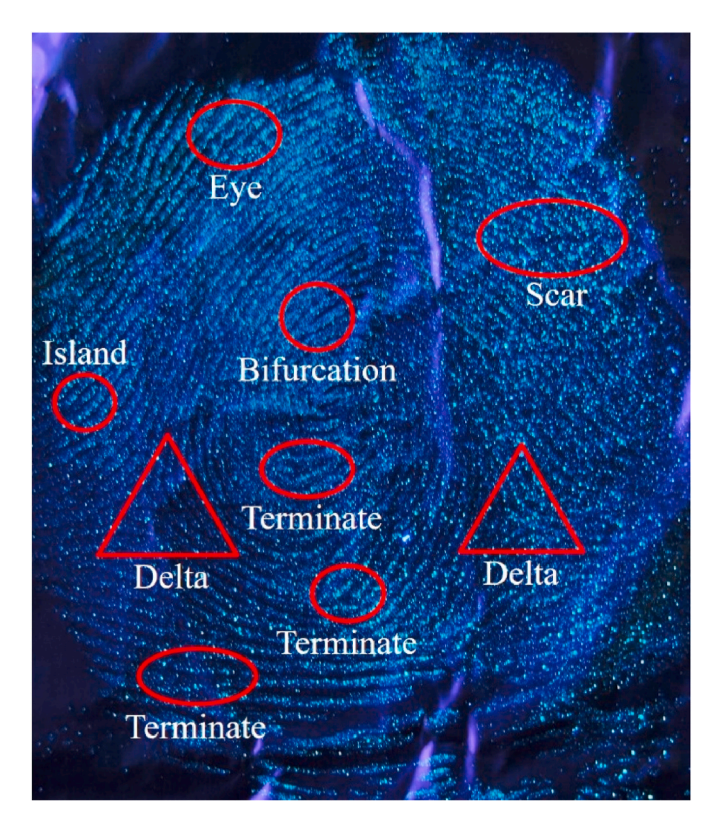


Fig. 12. The pattern images of LFP identification for fingerprint detection of $Sr_2MgSi_2O_7$: $4mol\%Eu^{2+}$ phosphor print on the surface of uneven aluminum foil.

efficiency was approximately 30%. The phosphor has excellent thermal stability, and its calculated activation energy (0.4051 eV) is higher than that of the general host material. This phosphor undergoes a linear decay with respect to the heating temperature, indicating its potential for application in temperature sensing. This phosphor powder can indicate the details of fingerprints on different surfaces, so it is considered as a promising candidate for identifying LFPs.

According to our DFT calculated results, Eu^{2+} doping has a significant effect on the electron orbitals of Si and O atoms; however, it does not influence the electron orbitals of Sr and Mg atoms. This means that the electronic flow is from the $\mathrm{Si}_2\mathrm{O}_7$ framework to the Eu^{2+} ion. The oxygen vacancy V_0 not only causes changes in the electron orbitals of Si and O atoms but also changes the orbitals of Sr atoms. Regardless of the Eu^{2+} doping, the oxygen vacancy V_0 has no effect on the electron orbits of Mg atoms. The oxygen vacancy V_0 caused almost no change in the s, p, and f electron orbitals of the Eu^{2+} ion; only its 5d empty orbit was changed.

Declaration of competing interest

We confirm that there are no known conflicts of interest associated with this publication and there has been no significant financial support for this work that could have influenced its outcome.

Acknowledgments

The authors would like to thank the Ministry of Science and Technology of the Republic of China, Taiwan, for financially supporting this research under contract No. MOST 109-2221-E-992-087.

Appendix A. Supplementary data

Supplementary data to this article can be found online at https://doi.

org/10.1016/j.jlumin.2020.117787.

References

- [1] J.K. Park, K.J. Choi, C.H. Kim, H.D. Park, S.Y. Choi, Optical properties of Eu²⁺-activated Sr₂SiO₄ phosphor for light-emitting diodes, Electrochem. Solid State Lett. 7 (2004). H15.
- [2] J. Zhang, G. Chen, H. Chen, Z. Zhai, Luminescence of Sr₂MgSi₂O_{7-1.5x}N_x: Eu²⁺, Dy³ phosphors with long afterglow properties for white LEDs, Opt. Mater 88 (2019) 333–338.
- [3] W. Wang, Z. Jiang, R. Wu, C. Li, R. Yao, X. Wei, T. Guo, J. Fan, L. Ni, L. Duan, Tunable luminescence of (Sr_{1-x}Ca_x)_{1,97}MgSi₂O₇: 0.03Eu²⁺ solid solution phosphors for cirtopic LEDs, Mater. Res. Express 6 (2019) 106206.
- [4] H. Wu, Y. Hu, L. Chen, X. Wang, Enhancement on the afterglow properties of Sr₂MgSi₂O₇: Eu²⁺ by Er³⁺ codoping, Mater. Lett. 65 (2011) 2676–2679.
- [5] O. Hai, Q. Ren, X. Wu, Q. Zhang, Z. Zhang, Z. Zhang, Insights into the element gradient in the grain and luminescence mechanism of the long afterglow material Sr₂MgSi₂O₇: Eu²⁺, Dy³⁺, J. Alloy. Comp 779 (2019) 892–899.
- [6] H. Wu, Y. Hu, Y. Wang, B. Zeng, Z. Mou, L. Deng, W. Xie, Influence on luminescent properties of the Sr₂MgSi₂O₇: Eu²⁺ by Dy³⁺, Nd³⁺ co-doping, J. Alloy. Comp 486 (2009) 549–553.
- [7] H. Wu, Y. Hu, X. Wang, Investigation of the trap state of Sr₂MgSi₂O₇: Eu²⁺, Dy³⁺ phosphor and decay process, Radiat. Meas 46 (2011) 591–594.
- [8] J. Zhang, Y. Li, Y. Wang, Y. Zhu, Microstructure and spectral characteristics of spectrum-fingerprint fiber with double luminous centers for anti-counterfeiting application, Appl. Optic. 59 (2020) 2004–2010.
- [9] L. Pan, S. Liu, X. Zhang, O. Oderinde, F. Yao, G. Fu, Optimization method for blue Sr₂MgSi₂O₇: Eu²⁺, Dy³⁺ phosphors produced by microwave synthesis route, J. Alloys Compd. 737 (2018) 39–45.
- [10] I.P. Sahu, D.P. Bisen, N. Brahme, M. Ganjir, Enhancement of the photoluminescence and long afterglow properties of Sr₂MgSi₂O₇: Eu²⁺ phosphor by Dy³⁺ co-doping, Luminescence 30 (2015) 1318–1325.
- [11] B.C. Babu, B.V. Rao, M. Ravi, S. Babu, Structural, microstructural, optical, and dielectric properties of Mn²⁺: willemite Zn₂SiO₄ nanocomposites obtained by a solgel method, J. Mol. Struct. 1127 (2017) 6–14.
- [12] O. Hai, E. Yang, Q. Ren, X. Wu, Y. Ren, Y. Zhao, J. Zhu, Enhancement of the persistent luminescence of Sr₂MgSi₂O₇: Eu²⁺, Dy³⁺ by Cu nanoparticles, J. Lumin 220 (2020) 116965.
- [13] G. Cui, X. Yang, Y. Zhang, Y. Fan, P. Chen, H. Cui, Y. Liu, X. Shi, Q. Shang, B. Tang, Round-the-Clock photocatalytic hydrogen production with high efficiency by a long-afterglow material, Angew. Chem. Int. Ed. 58 (2019) 1340–1344.
- [14] L. Zhang, H. Wu, Y. Jin, H. Sun, D. Liu, Y. Lv, G. Ju, L. Chen, Y. Hu, Competition of luminescence and photocatalysis in melilite: recombination and transportation of electrons. Physica B 573 (2019) 87–91.
- [15] C. Zhao, Y.H. Wu, D.H. Wang, S.X. Cao, S.Y. Chen, L.L. Peng, D.C. Zhu, A near-ultraviolet (NUV) converting blue-violet Mg₂SiO₄:Ce³⁺ phosphor for white light-emitting-diodes (w-LEDs), J. Lumin. 207 (2019) 241–245.
- [16] O. Hai, E. Yang, D. Li, W. Bai, Q. Ren, X. Wu, Plasma effect: a simple method for improving the persistent luminescence and light response range of persistent luminescent materials, J. Lumin. 217 (2020) 116785.
- [17] H. Cao, M. Liu, H. Chen, The luminescent properties of long afterglow phosphors: Ca₂MgSi₂O₇: Eu²⁺, Tm³⁺ with different preparation temperatures, Physica B 571 (2019) 243–246.
- [18] D. Singh, S. Sheoran, J. Singh, Optical characterization of ${\rm Eu}^{3+}$ doped MLSiO₄ (M = Ca, Sr, Ba and L = Mg) phosphor materials for display devices, J. Mater. Sci. Mater. Electron. 29 (2018) 294.
- [19] X. Wang, F. Li, G. Zuo, Y. Shen, F. Li, Enhanced afterglow properties of Nd³⁺ co-doped Sr2MgSi2O7: Eu2+, Dy3+ synthesized by sol–gel method, Ceram. Int. 42 (2016) 19441–19444.
- [20] L. Li, R. Zeng, H. Wang, Ba1.3Ca0.7SiO4: Eu2+, Mn2+: a white-lighting-emitting phosphor with extra afterglow properties via YF3 addition, J. Alloys Compd. 765 (2018) 249–252.
- [21] J.M. de Carvalho, D.V. der Heggen, L.I.D.J. Martin, P.F. Smet, Microwave-assisted synthesis followed by a reduction step: making persistent phosphors with a large storage capacity, Dalton Trans. 49 (2020) 4518–4527.
- [22] Y. Gong, Y. Wang, X. Xu, Y. Li, S. Xin, L. Shi, The persistent energy transfer of Eu²⁺ and Mn²⁺ and the thermoluminescence properties of long-lasting phosphor Sr₃MgSi₂O₈: Eu²⁺, Mn²⁺, Dy³⁺, Opt. Mater 33 (2011) 1781–1785.
- [23] C. Liu, X. Zhu, Z. Zhou, Effects of composition modulation on the structural and luminescence properties of Mn²⁺ doped Na₂Mg_{1-x}Ca_xSiO₄ greenemitting phosphors, Optics 179 (2019) 875–882.
- [24] S. Thomas, J.M. Kalita, M.L. Chithambo, O.M. Ntwaeaborwa, The influence of dopants on thermoluminescence of Sr₂MgSi₂O₇, J. Lumin. 208 (2019) 104–107.
- [25] O. Hai, H. Jiang, D. Xu, M. Li, The effect of grain surface on the long afterglow properties of Sr₂MgSi₂O₇: Eu²⁺, Dy³⁺, Mater. Res. Bull. 76 (2016) 358–364.
- [26] S. Li, S. Qi, K. Liu, H. Yuan, X. Sun, Influence of nitridation on optical properties of Sr₂MgSi₂O7: Eu2+ phosphors, Ceram. Int. 45 (2019) 20967–20971.
- [27] C. Yang, L. Xie, Q. Xiao, G. Liu, W. Peng, J. Meng, Ba1-xSrxMgSiO4: Eu2+, Mn2+: a novel tunable single-matrix tricolor phosphor for W-LED, J. Rare Earths 30 (2012) 110–113.
- [28] T. Aitasalo, J. Hassinen, J. Hölsä, T. Laamanen, M. Lastusaari, M. Malkamäki, J. Niittykoski1, P. Novák, Synchrotron radiation investigations of the Sr₂MgSi₂O₇: Eu²⁺, R³⁺ persistent luminescence materials, J. Rare Earths 27 (2009) 529–538.

- [29] J. Luo, Q. Gao, K. Zhang, M. Ge, J. Liu, Structure and luminescent properties of luminous polypropylene fiber based on Sr₂MgSi₂O₇:Eu²⁺, Dy³⁺, J. Rare Earths 32 (2014) 696–701.
- [30] R. Shrivastava, J. Kaur, Characterisation and mechano-luminescence studies of Sr₂MgSi₂O₇: Eu²⁺, Dy³⁺, J. Radiat. Res. Appl. Sci. 8 (2015) 201–207.
- [31] T.T.H. Tam, N.D. Hung, N.T.K. Lien, N.D.T. Kien, P.T. Huy, Synthesis and optical properties of red/blue-emitting Sr₂MgSi₂O₇: Eu³⁺/Eu²⁺ phosphors for white LED, J. Sci.: Adv. Mater. Devices 1 (2016) 204–208.
- [32] J. Hölsä, T. Laamanen, M. Lastusaari, P. Novák, Isolated defects in Sr₂MgSi₂O₇: a DFT study, Physics Procedia 29 (2012) 76–85.
- [33] I.P. Sahu, D.P. Bisen, N. Brahme, L. Wanjari, R. Tamrakar, Luminescence properties of Sr₂MgSi₂O₇: Eu²⁺, Ce³⁺ phosphor by solid state reaction method, Physics Procedia 76 (2015) 80–85.
- [34] A. Maghsoudipour, M.H. Sarrafi, F. Moztarzadeh, A.A. Bazazi, Influence of boric acid on properties of Sr₂MgSi₂O₇:Eu²⁺, Dy³⁺ phosphors, Pigment Resin Technol. 39 (2010) 32–35.
- [35] Y. Wang, X. Yang, Q. Ma, J. Kong, H. Jia, Z. Wang, M. Yu, Preparation of flower-like CdS with SDBS as surfactant by hydrothermal method and its optical properties, Appl. Surf. Sci. 340 (2015) 18–24.
- [36] Y. Wang, Q. Ma, H. Jia, Z. Wang, One-step solution synthesis and formation mechanism of flower-like ZnO and its structural and optical characterization, Ceram. Int. 42 (2016) 10751–10757.
- [37] Y. Wang, D. Wang, B. Yan, Y. Chen, C. Song, Fabrication of diverse CuO nanostructures via hydrothermal method and their photocatalytic properties, J. Mater. Sci. Mater. Electron. 27 (2016) 6918–6924.
- [38] X. Yang, Y. Wang, Z. Wang, X. Lv, H. Jia, J. Kong, M. Yu, Preparation of CdS/TiO₂ nanotube arrays and the enhanced photocatalytic property, Ceram. Int. 42 (2016) 7192–7202
- [39] X. Yang, Z. Wang, X. Lv, Y. Wang, H. Jia, Enhanced photocatalytic activity of Zndoped dendritic-like CdS structures synthesized by hydrothermal synthesis, J. Photochem. Photobiol. A 329 (2016) 175–181.
- [40] A. Tymiński, E. Śmiechowicz, I.R. Martín, T. Grzyb, Ultraviolet- and near-infraredexcitable LaPO4:Yb3+/Tm3+/Ln3+ (Ln = Eu, Tb) nanoparticles for luminescent fibers and optical thermometers, ACS Appl. Nano Mater 3 (2020) 6541–6551.
- [41] H. Khajuria, M. Kumar, L. Tashi, R. Singh, H.N. Sheikh, Studies on morphology and photoluminescent properties of Tb³⁺ doped YbPO₄ nanostructures synthesized by different synthetic methods, Acta Chim. Slov 67 (2020) 119–129.
- [42] C. Malik, N. Kaur, B. Singh, A. Pandey, Luminescence properties of tricalcium phosphate doped with dysprosium, Appl. Radiat. Isot. 158 (2020) 109062.
- [43] N.T. Mandlik, P.D. Sahare, S.D. Dhole, Effect of size variation and gamma irradiation on thermoluminescence and photoluminescence characteristics of CaSO₄: Eu micro- and nanophosphors, Appl. Radiat. Isot. 159 (2020) 109080.
- [44] S. He, F. Xu, T. Han, Z. Lu, W. Wang, J. Peng, F. Du, F. Yang, X. Ye, A Mn⁴⁺-doped oxyfluoride phosphor with remarkable negative thermal quenching and high color stability for warm WLEDs., Chem. Eng. J. 392 (2020) 123657.
- [45] A. Cantarano, A. Ibanez, G. Dantelle, Garnet-type nanophosphors for white LED lighting. Front. Mater 7 (2020) 210.
- [46] M. Vallés-Pelarda, R.S. Sanchez, E.M. Barea, I. Mora-Seró, B. Julián-López, Up-Converting Lanthanide-doped YAG nanospheres, Front. Mater 7 (2020) 273.
- [47] Y. Wang, P. Darapaneni, O. Kizilkaya, J.A. Dorman, Role of Ce in manipulating the photoluminescence of Tb doped Y₂Zr₂O₇, Inorg. Chem. 59 (2020) 2358–2366.
- [48] F. Hong, H. Xu, G. Pang, G. Liu, X. Dong, W. Yu, Optical characteristics, morphology evolution and thermal stability of novel red-emitting Mn⁴⁺-activated K₂LiAl_{1-y}Ga_yF₆ solid solution phosphors for high-performance warm WLED, J. Allovs Compd. 824 (2020) 153818.
- [49] L. Mentasti, N. Martínez, I.A. Zucchi, M. Santiago, G. Barreto, Development of a simple process to obtain luminescent YVO₄:Eu³⁺ nanoparticles for Fiber Optic Dosimetry, J. Alloys Compd 829 (2020) 154628.
- [50] K. Thomas, D. Alexander, K.P. Mani, S. Gopi, S.A. Kumar, P.R. Biju, N. V. Unnikrishnan, C. Joseph, Intrinsic red luminescence of Eu³⁺-activated lanthanum molybdate: insights into the spectroscopic features using Judd–Ofelt theoretical analysis, J. Phys. Chem. Solid. 137 (2020) 109212.
- [51] W. Zhang, R. Zhang, S. Yang, R. Wang, L. Na, R. Hua, Synthesis and photoluminescent features of Eu³⁺-doped NaGd(WO₄)₂ nanophosphors, Mater. Res. Bull. 122 (2020) 110689.
- [52] Z. Li, L. Li, H. Liu, F. Li, J. Zhao, Y. Wang, Strongly quantum-confined Mn²⁺- doped CsPbBr₃ nanocrystals in MCM-41 with pure blue emission, New J. Chem. 44 (2020) 2980
- [53] K. Ren, X. Wu, H. Zhang, J. Li, Ultrathin (Y_{0.98}Re_{0.02})₂(OH)₅NO₃· nH₂O (Re = Pr, Sm, Eu, Tb, Dy, Ho, Er, Tm) nanosheets and well-dispersed oxide nanoparticles: facile co-precipitation synthesis and multi-color luminescent properties, Opt. Mater. 105 (2020) 109884.

- [54] P. Hohenberg, W. Kohn, Inhomogeneous electron gas, Phys. Rev. 136 (1964) B864–B871.
- [55] W. Kohn, L.J. Sham, Self-consistent equations including exchange and correlation effects, Phys. Rev. 140 (1965) A1133–A1138.
- [56] M.C. Payne, M.P. Teter, D.C. Allan, T.A. Arias, J.D. Joannopoulos, Iterative minimization techniques for ab initio total-energy calculations - moleculardynamics and conjugate gradients, Rev. Mod. Phys. 64 (1992) 1045–1097.
- [57] S.J. Clark, M.D. Segall, C.J. Pickard, P.J. Hasnip, M.J. Probert, K. Refson, M. C. Payne, First principles methods using {CASTEP}, Z. Kristallogr. 220 (2005) 567–570.
- [58] B.G. Pfrommer, M. Cote, S.G. Louie, M.L. Cohen, Relaxation of crystals with the quasi-Newton method, J. Comput. Phys. 131 (1997) 233–240.
- [59] H.J. Monkhorst, J.D. Pack, Special points for Brillouin-zone integrations, Phys. Rev. B 13 (1976) 5188–5192.
- [60] S. Zhou, H. Wang, L. Zhong, J. Zhao, L. Lic, G. Li, Synthesis and photoluminescence of Ca_{1.x}TiO₃: xEu3+ nanoparticles, J. Mater. Sci. Technol. 34 (2018) 949–954.
- [61] Y. Lin, J. Zhou, Z. Qiu, W. Zhou, J. Zhang, C. Li, L. Yu, S. Lian, To tune europium valence by controlling the composition in diphase silicate phosphors, J. Rare Earths 36 (2018) 1015–1023.
- [62] I.P. Sahu, D.P. Bisen, R.K. Tamrakar, K.V.R. Murthy, M. Mohapatra, Luminescence studies on the europium doped strontium metasilicate phosphor prepared by solid state reaction method, J. Sci.: Adv. Mater. Devices 2 (2017) 59–68.
- [63] J. Huang, R. Liu, Y. Liu, Y. Hu, G. Chen, C. Yan, J. Tian, B. Hu, Effect of fluxes on synthesis and luminescence properties of BaSi₂O₂N₂:Eu²⁺ oxynitride phosphors, J. Rare Earths 36 (2018) 225–230.
- [64] H. Duan, Y.Z. Dong, Y. Huang, Y.H. Hu, X.S. Chen, The important role of oxygen vacancies in Sr₂MgSi₂O₇ phosphor, Phys. Lett. A 380 (2016) 1056–1062.
- [65] O. Hai, E. Yang, B. Wei, Q. Ren, X. Wu, J. Zhu, The trap control in the long afterglow luminescent material (Ca, Sr)₂MgSi₂O₇: Eu²⁺, Dy³⁺, J. Solid State Chem 283 (2020) 121174.
- [66] S.J. Park, J.Y. Park, H.K. Yang, Luminescence of a novel cyan emitting Sr10(PO4) 6O: Ce3+ phosphor for visualization of latent fingerprints and anti-counterfeiting applications, Sensor. Actuator. B Chem. 262 (2018) 542–554.
- [67] F. Femila Komahal, H. Nagabhushana, R.B. Basavaraj, G.P. Darshan, H.K. Inamdar, S.C. Sharma, B. Daruka Prasad, Rational design of monovalent ions (Li, Na, K) codoped ZnAl₂O₄:Eu³⁺ nanocrystals enabling versatile robust latent fingerprint visualization, J. Rare Earths 37 (2019) 699–705.
- [68] R.S.P. King, L.W.L. Davis, D.A. Skros, The use of longwave reflected UV imaging for the enhancement of cyanoacrylate developed fingermarks: a simple, safe and effective imaging tool, Forensic Sci. Int. 289 (2018) 329–336.
- [69] H.J. Wang, T.T. Yu, H.L. Chen, W.B. Nan, L.Q. Xie, Q.Q. Zhang, A self-quenching-resistant carbon dots powder with tunable solid-state fluorescence and their applications in light-emitting diodes and fingerprints detection, Dyes Pigments 159 (2018) 245–251.
- [70] G.S. Bumbrah, Small particle reagent (SPR) method for detection of latent fingermarks: a review, Egypt. J. Forensic Sci 6 (2016) 328–332.
- [71] J. Shao, J. Yan, X. Li, S. Li, T. Hu, Novel fluorescent label based on YVO4: Bi3+, Eu3+ for latent fingerprint detection, Dyes Pigments 160 (2019) 555–562.
- [72] K.R. Venkatesha Babu, C.G. Renuka, R.B. Basavaraj, G.P. Darshan, H. Nagabhushana, One pot synthesis of TiO₂:Eu³⁺ hierarchical structures as a highly specific luminescent sensing probe for the visualization of latent fingerprints, J. Rare Earths 37 (2019) 134–144.
- [73] M. Dhanalakshmi, H. Nagabhushana, G.P. Darshan, R.B. Basavaraj, B. Daruka Prasad, Sonochemically assisted hollow/solid BaTiO₃:Dy³⁺ microspheres and their applications in effective detection of latent fingerprints and lip prints, J. Sci.: Adv. Mater. Devices 2 (2017) 22–33.
- [74] C. Suresh, H. Nagabhushana, G.P. Darshan, R.B. Basavaraj, D. Kavyashree, S. C. Sharma, A. Arulmozhi, B. Daruka Prasad, H.J. Amith Yadav, Facile LaOF: Sm³⁺ based labeling agent and their applications in residue chemistry of latent fingerprint and cheiloscopy under UV-visible light, Arabian J. Chem. 11 (2018) 460-482.
- [75] M. Venkataravanappa, R.B. Basavaraj, G.P. Darshan, B. Daruka Prasad, S. C. Sharma, P. Hema Prabha, S. Ramani, H. Nagabhushana, Multifunctional Dy (III) doped di-calcium silicate array for boosting display and forensic applications, J. Rare Earths 36 (2018) 690–702.
- [76] R.B. Basavaraj, G.P. Darshan, B. Daruka Prasad, S.C. Sharma, H. Nagabhushana, Rapid visualization of latent fingerprints using novel CaSiO₃:Sm³⁺ nanophosphors fabricated via ultrasound route, J. Rare Earths 37 (2019) 32–44.
- [77] S.H. Yang, Y.C. Hung, P.C. Tseng, H.Y. Lee, Versatile deep-red Mg₂TiO₄:Mn⁴⁺ phosphor for photoluminescence, thermometry, and latent fingerprint visualization, J. Alloys Compd. 801 (2019) 394–401.